



## Realization of Translational Symmetry in Trapped Cold Ion Rings

Hao-Kun Li,<sup>1</sup> Erik Urban,<sup>2</sup> Crystal Noel,<sup>2</sup> Alexander Chuang,<sup>2</sup> Yang Xia,<sup>1</sup> Anthony Ransford,<sup>2</sup> Boerge Hemmerling,<sup>2</sup> Yuan Wang,<sup>1,3</sup> Tongcang Li,<sup>1</sup> Hartmut Häffner,<sup>2,3,†</sup> and Xiang Zhang<sup>1,3,\*</sup>

<sup>1</sup>*Nanoscale Science and Engineering Center, University of California, Berkeley, California 94720, USA*

<sup>2</sup>*Department of Physics, University of California, Berkeley, California 94720, USA*

<sup>3</sup>*Materials Sciences Division, Lawrence Berkeley National Laboratory, 1 Cyclotron Road, Berkeley, California 94720, USA*

(Received 17 June 2016; published 31 January 2017)

We crystallize up to 15  $^{40}\text{Ca}^+$  ions in a ring with a microfabricated silicon surface Paul trap. Delocalization of the Doppler laser-cooled ions shows that the translational symmetry of the ion ring is preserved at millikelvin temperatures. By characterizing the collective motion of the ion crystals, we identify homogeneous electric fields as the dominant symmetry-breaking mechanism at this energy scale. With increasing ion numbers, such detrimental effects are reduced. We predict that, with only a ten-ion ring, uncompensated homogeneous fields will not break the translational symmetry of the rotational ground state. This experiment opens a door towards studying quantum many-body physics with translational symmetry at the single-particle level.

DOI: 10.1103/PhysRevLett.118.053001

Spontaneous symmetry breaking is a universal concept throughout physics. For instance, the Landau-Ginzburg paradigm of translational symmetry breaking underlies the classification of nearly all quantum phases of matter and explains the emergence of crystals, insulators, and superconductors [1]. Usually, the consequences of translational invariance are studied in large systems (e.g., condensed matter systems [2] and optical lattices [3]) to suppress edge effects which cause undesired symmetry breaking. While this approach works for investigating global properties, studies of local observables and their correlations require access and control of the individual constituents. Through the implementation of periodic boundary conditions, one can hope to realize translational symmetry in small systems where single-particle control is achievable.

Rings of trapped ions with inherent periodic boundary conditions offer a large degree of control down to the single-particle level [4–10]. However, it has been a long-standing experimental challenge to restore the translational symmetry of ion rings. In previous experiments, the ion-electrode distances have been much smaller than the ion-ring diameters, making the ring sensitive to complex stray electric fields from nearby surfaces [10]. Although the stray fields do not significantly affect high-energy ion rings [9], they substantially disrupt the translational symmetry at low temperatures, where many interesting quantum phenomena can be observed. Hence, it is desirable to reduce the ion-ring diameter while keeping the ions far away from the electrodes, such that stray fields from imperfections vary on length scales larger than the ring diameter. This strategy avoids local distortions of the ion ring.

In this Letter, using a novel trap design [11,12], we crystallize  $^{40}\text{Ca}^+$  ions in a 90  $\mu\text{m}$  diameter ring with 390  $\mu\text{m}$  ion-electrode distance. In our experiment,

unavoidable stray electric fields can be compensated with primarily homogeneous fields. For the first time, we show that the translational symmetry of the ion ring is preserved at millikelvin temperatures by delocalizing the Doppler laser-cooled ions. This establishes an upper bound for undesired symmetry breaking at a level where quantum control becomes feasible. Our experiment paves the way towards studying quantum many-body physics with translational symmetry at the single-particle level in a variety of disciplines from the simulation of Hawking radiation [13] to the exploration of quantum phase transitions [14]. In addition, the ring geometry enables novel opportunities to study diverse topics including dynamics of kink solitons [15,16], the Kibble-Zureck mechanism [17–19], the Aharonov-Bohm effect [20], symmetry breaking with indistinguishable particles [21,22], frequency metrology [23], quantum friction [24], and quantum computation [25].

Our ring trap consists of three concentric circular electrodes surrounded by eight static-voltage compensation electrodes, as shown in Fig. 1(a). Applying a radio-frequency (rf) voltage to the innermost and outermost circular electrodes with all other electrodes held at a dc voltage generates a time-averaged circular potential minimum above the trap surface [12]. The trap is fabricated from boron-doped silicon anodically bonded on borofloat glass ( $\text{SiO}_2$ ) [26], as shown in Fig. 1(b). The electrodes are formed using photolithography followed by deep dry etching of silicon. The deep electrode trenches shown in Fig. 1(c) ensure that stray fields from bound charges in the glass are well shielded. Hydrofluoric acid (HF) etching of the glass underneath the trenches is performed to increase the distance between the electrodes through the glass surface. This process prevents surface breakdown when a high voltage is applied between neighboring electrodes

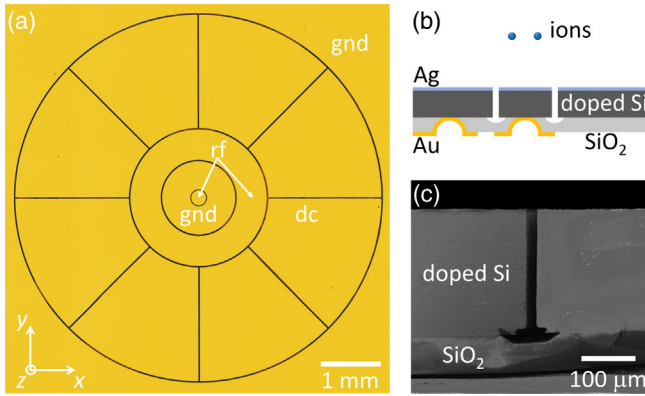


FIG. 1. (a) Optical image of the trap electrodes illuminated with yellow light. The trap consists of three circular electrodes and eight static voltage electrodes in a plane. The outer radius of the three circular electrodes are 125, 600, and 1100  $\mu\text{m}$ , respectively. The gap between the innermost and the next circular electrode is 15  $\mu\text{m}$ , and the gaps between other electrodes are 25  $\mu\text{m}$ . The whole electrode pattern possesses a diameter of 6 mm, outside of which is ground. (b) Cross-sectional schematics of the fabricated trap. The resistivity of the doped silicon is  $< 0.005\text{ ohm cm}$ . The thickness of the Ag, Si, and SiO<sub>2</sub> layers are 100 nm, 250  $\mu\text{m}$ , and 70  $\mu\text{m}$ , respectively. Electrical vias through the SiO<sub>2</sub> layer are coated with an 800 nm layer of gold. (c) Scanning electron microscope image of the trap cross section.

[27]. In the interest of leaving the potential above the trap undisturbed, electrical vias are created on the backside by HF etching of the glass substrate, followed by gold deposition and a lift-off process.

The ring trap is operated by applying a 220 V amplitude,  $2\pi \times 5.81\text{ MHz}$  signal to the rf electrodes. A flux of neutral calcium atoms generated from a heated atom oven travels parallel to the trap surface. The neutral calcium is then ionized inside the trapping region through a two-photon process at 422 and 375 nm. A red-detuned 397 nm laser beam then cools the ions, while an 866 nm laser beam repumps the ions out of the dark  $D$  state [28]. The fluorescence of the ions at 397 nm is collected with a custom objective [29] and imaged upon an electron-multiplying charge-coupled device (EMCCD) camera.

When captured by the trapping potential, the ions crystallize into a ring because of their mutual Coulomb repulsion, as shown in Fig. 2. With no compensating fields applied, the ions are typically pinned to one side of the ring by stray electric fields. The strength of the stray fields in the  $xy$  plane is measured to be 3 V/m by recording the compensating field required to reposition the ion crystal to be first  $x$  and then  $y$  axis symmetric. A local field due to a quadrupole moment of the order of 1 V/m is also present (expressed as the product of the quadrupole moment and ring radius). These stray fields are compensated for by using the static voltage compensation electrodes before applying additional fields throughout the extent of this Letter. The measured radial trapping frequency is

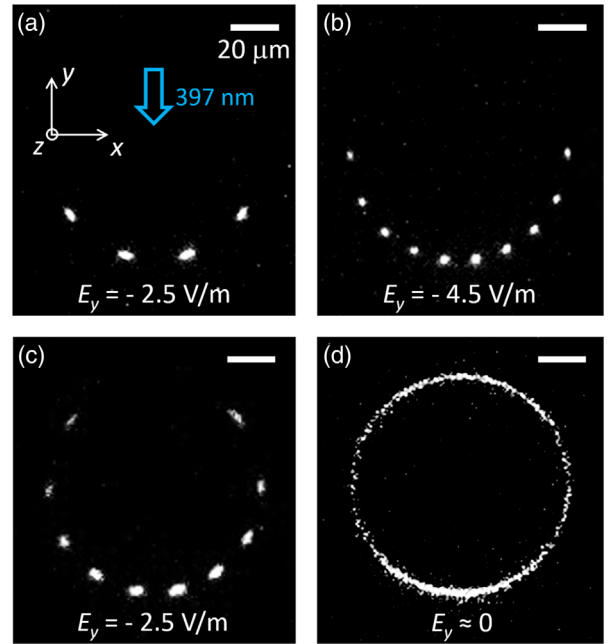


FIG. 2. (a)–(c) Images of ion crystals composed of four ions (a) and ten ions (b),(c) for different total dipole fields  $E_y$ . (d) Image of a delocalized ten-ion ring when the total external dipole field is close to zero (exposure time 200 ms). In (a)–(d), the scale bars are 20  $\mu\text{m}$ . The fluorescence inhomogeneity of the images is caused by the size of the Gaussian cooling beam of  $\sim 70\text{ }\mu\text{m}$  full width at half maximum [30].

$2\pi \times 390\text{ kHz}$ . The trapping potential is able to hold up to 15 ions in a ring before the ion crystal forms a zigzag configuration when pinned.

The presence of external electric fields in the trapping plane creates an asymmetry in the ring potential, resulting in a finite tangential trapping frequency (direction defined along the circumference of the ring). We gauge the asymmetry by measuring the tangential trapping frequency of the ion crystal. In the measurement, we apply a sinusoidal voltage to one compensation electrode and observe the excitation of the collective tangential mode with the EMCCD camera. Figures 3(a) and 3(b) present the observed dependence of the tangential trapping frequency on the total external dipole field  $E_y$  and the ion number  $N$ , respectively. As the ion number becomes larger, the increased Coulomb repulsion resulting from the reduced ion-ion spacing enforces a more uniform charge distribution in the ring, as shown in Figs. 2(a) and 2(c). For such a homogeneous charge distribution, an external electric field exerts a smaller restoring torque when the ion crystals deviate from the equilibrium position. Therefore, we expect the tangential trapping frequencies to decrease with an increasing ion number and better compensation of the stray fields.

The potential energy of the ion crystals can be modeled by considering only a homogeneous external field and the Coulomb repulsion of the ions confined to a ring. This results in a potential energy of the form

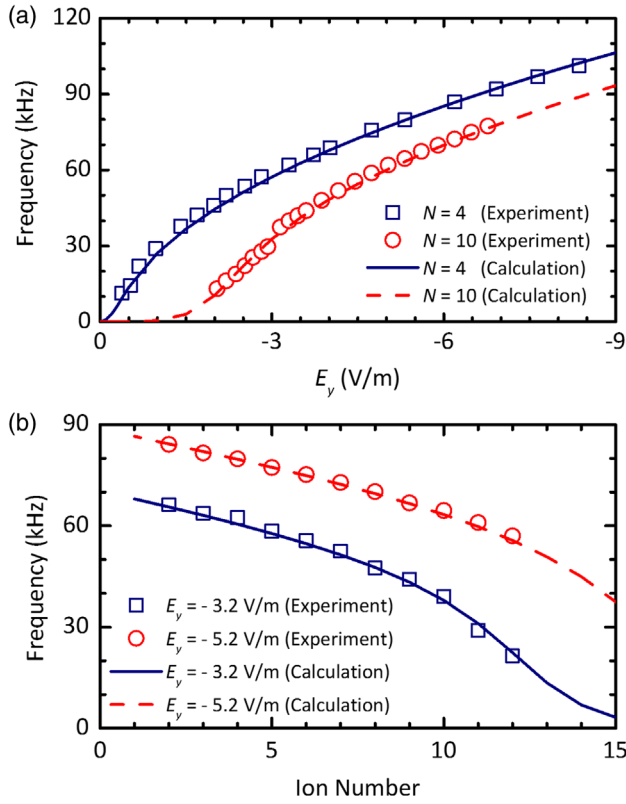


FIG. 3. Dependence of the tangential trapping frequency  $\omega_t$  on the total external dipole field strength  $E_y$  (a) and ion number  $N$  (b), respectively. Error bars are smaller than the sizes of the data points. The curves correspond to the calculated collective tangential frequencies using the electric potential model considering only a homogeneous electric field and the Coulomb repulsion of the ions confined to a ring. The agreement between the calculated results and the experimental data confirms that the homogeneous electric fields are the dominant symmetry-breaking mechanism.

$$V = -\sum_i \frac{1}{2} E_y e d \cos \theta_i + \sum_{i < j} \frac{e^2}{4\pi\epsilon_0 d \sin \left| \frac{\theta_i - \theta_j}{2} \right|}, \quad (1)$$

where  $d$  denotes the ring diameter,  $\theta_i$  the angular position of the  $i$ th ion,  $e$  the elementary charge, and  $\epsilon_0$  the vacuum permittivity. We calculate the frequencies of the collective tangential motion by expanding the potential energy of the ion crystals to quadratic order in the ion displacements relative to equilibrium. The results are presented in Figs. 3(a) and 3(b). The calculation agrees with the experimental results over the full extent of the measurement without free fitting parameters. This result confirms that homogeneous electric fields are the dominant symmetry-breaking mechanism at the energy scales of our measurement. See Supplemental Material for the effects of residual quadrupole fields [30].

In order to quantify the scale at which the symmetry is broken, we use the magnitude of the perturbations of the potential that cause the localization of the ion ring, defined as

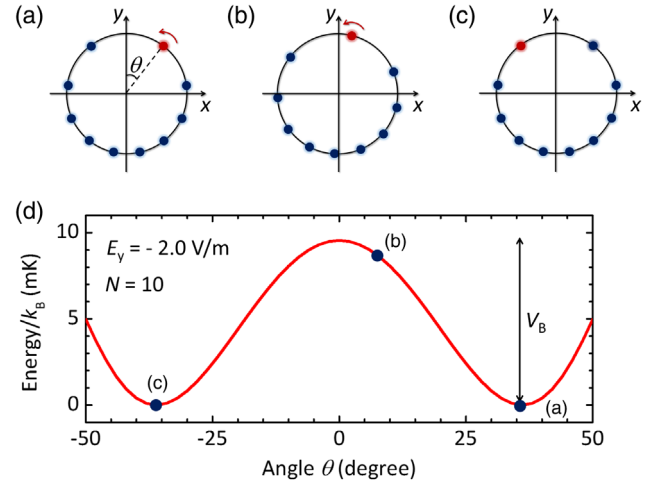


FIG. 4. The lowest potential energy configurations of a ten-ion crystal as a function of the position of the final ion (marked in red). The original equilibrium configuration is shown in (a). When the final ion moves from right to left, the nine other ions move into a new minimum configuration (b), and the crystal eventually recovers the original equilibrium configuration (c). (d) The calculated potential energy of ten ions as a function of the final ion position angle  $\theta$ , where the difference between the minimum and the maximum is the rotational energy barrier  $V_B$ . The marked points correspond to the equilibrium configurations shown in (a)–(c), respectively.  $E_y = -2.0$  V/m.

the rotational energy barrier. To obtain the rotational energy barrier, we numerically vary the position of the final ion in the chain and use the confirmed model presented in Eq. (1) to solve for the lowest potential energy configuration of the remaining ions, as described by Figs. 4(a)–4(c). The calculated potential energy of a ten-ion crystal versus the final ion position is plotted in Fig. 4(d). The two minimum energy locations correspond to the original equilibrium configuration of the crystal, and the energy peak represents the rotational energy barrier  $V_B$ . For ten ions, we observe localized ring crystals with in-plane electric fields larger than  $(2.0 \pm 0.1)$  V/m. At this electric field, the rotational energy barrier is calculated to be  $V_B/k_B = (10 \pm 4)$  mK, where  $k_B$  is the Boltzmann constant.

By decreasing the external field or increasing the ion number, the rotational energy barrier can be reduced to the point where the ion ring delocalizes, as shown in Fig. 2(d), where the ions no longer have a constant angular position. For a ten-ion crystal, delocalization occurs at  $E_y = -(1.9 \pm 0.1)$  V/m corresponding to a rotational energy barrier of  $V_B/k_B = (6 \pm 3)$  mK. As more ions are held in the trap, the field strength at which the ring delocalizes increases, as shown in Fig. 5(a). This trend is due to the fact that increased Coulomb repulsion from more ions increases the force necessary to deform the ring. The delocalization point is sensitive to the position of the cooling beam. The radiation pressure from an unbalanced cooling beam exerts a net torque on the ring, leading to a delocalization at larger

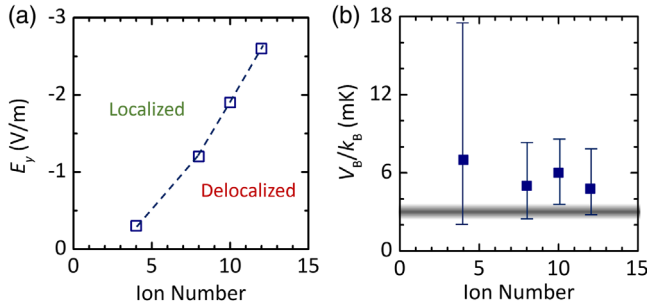


FIG. 5. Total external electric field strength (a) and corresponding rotational energy barrier  $V_B/k_B$  (b) at which the ion crystals are observed to delocalize as a function of the ion number. The errors of the electric fields in (a) are  $\pm 0.1$  V/m. The gray line in (b) denotes the measured tangential temperature  $\sim 3$  mK of the ions, which is close to  $V_B/k_B$ , and suggests that the delocalization occurs when the thermal energy of the ions is large enough to overcome the rotational energy barrier.

fields. For this reason, the cooling laser is positioned to the point at which the transition occurs at the smallest field.

Though the field at which the ring delocalizes increases with an increased ion number, we find that the corresponding rotational energy barrier is independent of the ion number, as shown in Fig. 5(b). We determine the tangential temperature of the ions to be  $\sim 3$  mK by measuring the Doppler-broadened width of the 729 nm  $4^2S_{1/2}$ - $3^2D_{5/2}$  transition [28]. The proximity of the ion temperature to  $V_B/k_B$  suggests that delocalization occurs when the tail of the Boltzmann distribution of the ions is large enough to overcome the rotational energy barrier. This hypothesis is confirmed by comparing the observed delocalized distribution of the ions with a simulation employing the Langevin equation to include the stochastic effect of temperature in the ion dynamics as is shown in Fig. 6 [30]. The agreement of the simulated angular ion distribution and the experimental data shows that all relevant interactions have been taken into account and that delocalization is well described solely by thermal effects corresponding to the measured temperature.

Ultimate control of the ion ring requires translational symmetry of its rotational ground state in the picokelvin regime [22]. In the future, we look to explore what mechanism could break the symmetry at energy scales below the Doppler limit studied here. So far, we have found that the main symmetry-breaking mechanism is homogeneous fields. From our model, we estimate that, with our achieved control of  $\sim 0.1$  V/m, homogeneous fields will not affect the symmetry of a ten-ion ring even at the  $10^{-12}$  K level. Approaching these small energies, we expect that higher order multipole fields will become relevant [30]. To explore these effects, further cooling of the rotational degree of freedom is required.

In summary, we have implemented a ring of  $^{40}\text{Ca}^+$  ions with a novel trap design. Unavoidable symmetry-breaking stray fields can be compensated with primarily homogeneous

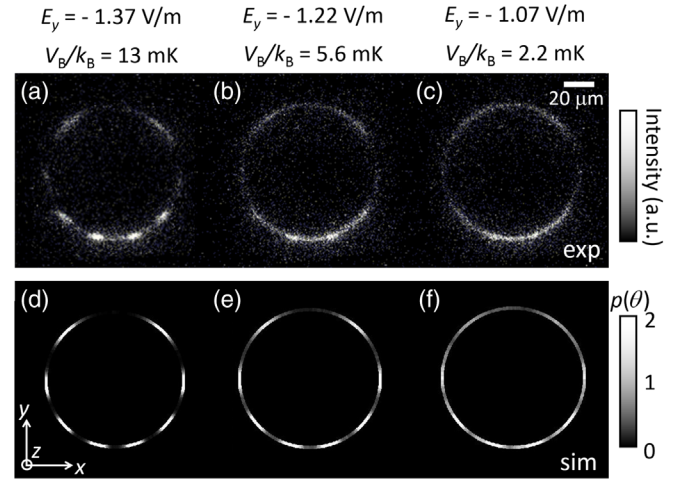


FIG. 6. (a)–(c) Image of eight-ion rings in the localization-delocalization transition regime. (d)–(f) Corresponding simulated angular distribution  $p(\theta)$  of the ions using the Langevin equation at 3 mK. The dipole electric fields  $E_y$  and the corresponding rotational energy barriers  $V_B/k_B$  are  $-1.37$ ,  $-1.22$ , and  $-1.07$  V/m and 13, 5.6, and 2.2 mK for (a) and (d), (b) and (e), and (c) and (f), respectively. As in Fig. 2, reduced fluorescence on the extrema of the  $x$  axis is due to the Gaussian profile of the detection beam incident from the positive  $y$  direction.

fields to provide a high degree of translational symmetry. The translational invariance of the ion ring is preserved at millikelvin temperatures and can be potentially maintained much further. Our system opens up a new experimental regime to explore many-body quantum physics with translational invariance where individual particles can be accessed and controlled. In addition, the symmetry and periodicity of the ion ring provide a unique platform in which to explore quantum computing and quantum simulation.

The design and characterization of this work is supported by the W. M. Keck Foundation; the fabrication is supported by the Director, Office of Science, Office of Basic Energy Sciences, Materials Sciences and Engineering Division, of the U.S. Department of Energy under Contract No. DE-AC02-05-CH11231. E. U. acknowledges support by the NSF Graduate Research Fellowship under Grant No. 1106400. The authors thank Norman Yao for helpful discussions.

H.-K. L. and E. U. contributed equally to this work.

\*Corresponding author.  
xiang@berkeley.edu

†Corresponding author.  
hhaeffner@berkeley.edu

- [1] L. D. Landau and E. Lifshitz, *Statistical Physics* (Elsevier, New York, 2013), Vol. 5.
- [2] P. W. Anderson, *Basic Notions of Condensed Matter Physics*, 2nd ed. (Westview, Boulder, CO, 1997).

- [3] I. Bloch, *Nat. Phys.* **1**, 23 (2005).
- [4] D. Leibfried, R. Blatt, C. Monroe, and D. Wineland, *Rev. Mod. Phys.* **75**, 281 (2003).
- [5] H. Häffner, C. Roos, and R. Blatt, *Phys. Rep.* **469**, 155 (2008).
- [6] R. Blatt and C. F. Roos, *Nat. Phys.* **8**, 277 (2012).
- [7] I. Waki, S. Kassner, G. Birkel, and H. Walther, *Phys. Rev. Lett.* **68**, 2007 (1992).
- [8] G. Birkel, S. Kassner, and H. Walther, *Nature (London)* **357**, 310 (1992).
- [9] T. Schätz, U. Schramm, and D. Habs, *Nature (London)* **412**, 717 (2001).
- [10] B. Tabakov, F. Benito, M. Blain, C. R. Clark, S. Clark, R. A. Haltli, P. Maunz, J. D. Sterk, C. Tigges, and D. Stick, *Phys. Rev. Applied* **4**, 031001 (2015).
- [11] R. J. Clark, *Appl. Phys. B* **113**, 171 (2013).
- [12] P.-J. Wang, T. Li, C. Noel, A. Chuang, X. Zhang, and H. Häffner, *J. Phys. B* **48**, 205002 (2015).
- [13] B. Horstmann, B. Reznik, S. Fagnocchi, and J. I. Cirac, *Phys. Rev. Lett.* **104**, 250403 (2010).
- [14] E. Shimshoni, G. Morigi, and S. Fishman, *Phys. Rev. Lett.* **106**, 010401 (2011).
- [15] H. Landa, S. Marcovitch, A. Retzker, M. B. Plenio, and B. Reznik, *Phys. Rev. Lett.* **104**, 043004 (2010).
- [16] H. Landa, A. Retzker, T. Schaetz, and B. Reznik, *Phys. Rev. Lett.* **113**, 053001 (2014).
- [17] S. Ulm *et al.*, *Nat. Commun.* **4**, 2290 (2013).
- [18] K. Pyka *et al.*, *Nat. Commun.* **4**, 2991 (2013).
- [19] P. Silvi, G. Morigi, T. Calarco, and S. Montangero, *Phys. Rev. Lett.* **116**, 225701 (2016).
- [20] A. Noguchi, Y. Shikano, K. Toyoda, and S. Urabe, *Nat. Commun.* **5**, 3868 (2014).
- [21] F. Wilczek, *Phys. Rev. Lett.* **109**, 160401 (2012).
- [22] T. Li, Z.-X. Gong, Z.-Q. Yin, H. T. Quan, X. Yin, P. Zhang, L.-M. Duan, and X. Zhang, *Phys. Rev. Lett.* **109**, 163001 (2012).
- [23] C. Champenois, M. Marciante, J. Pedregosa-Gutierrez, M. Houssin, M. Knoop, and M. Kajita, *Phys. Rev. A* **81**, 043410 (2010).
- [24] A. Bylinskii, D. Gangloff, and V. Vuletić, *Science* **348**, 1115 (2015).
- [25] G.-D. Lin, S.-L. Zhu, R. Islam, K. Kim, M.-S. Chang, S. Korenblit, C. Monroe, and L.-M. Duan, *Europhys. Lett.* **86**, 60004 (2009).
- [26] D. Stick, W. K. Hensinger, S. Olmschenk, M. J. Madsen, K. Schwab, and C. Monroe, *Nat. Phys.* **2**, 36 (2006).
- [27] R. C. Sterling, H. Rattanasonti, S. Weidt, K. Lake, P. Srinivasan, S. C. Webster, M. Kraft, and W. K. Hensinger, *Nat. Commun.* **5**, 3637 (2014).
- [28] A. Kreuter *et al.*, *Phys. Rev. A* **71**, 032504 (2005).
- [29] L. M. Bennie, P. T. Starkey, M. Jasperse, C. J. Billington, R. P. Anderson, and L. D. Turner, *Opt. Express* **21**, 9011 (2013).
- [30] See Supplemental Material at <http://link.aps.org/supplemental/10.1103/PhysRevLett.118.053001> for residual quadrupole field analysis and Langevin dynamics simulation.